

Formation history and physical properties of sediments from the Mount Elbert Gas Hydrate Stratigraphic Test Well, Alaska North Slope

Sheng Dai, Changho Lee*, J. Carlos Santamarina

School of Civil and Environmental Engineering, Georgia Institute of Technology, Atlanta, GA 30332, USA

ARTICLE INFO

Article history:

Received 14 April 2009

Received in revised form

2 March 2010

Accepted 8 March 2010

Available online 15 March 2010

Keywords:

Mount Elbert

Permafrost

Gas hydrate

Seismic waves

Permittivity

Conductivity

Stress–volume response

Gas production

ABSTRACT

The synthesis of available geological information and surface temperature evolution in the Alaska North Slope region suggests that: biogenic and deeper thermogenic gases migrated through fault networks and preferentially invaded coarse-grained layers that have relatively high hydraulic conductivity and low gas entry pressures; hydrate started forming before the beginning of the permafrost; eventually, the permafrost deepened and any remaining free water froze so that ice and hydrate may coexist at some elevations. The single tested specimen (depth 620.47–620.62 m) from the D unit consists of uncemented quartzitic fine sand with a high fraction of fines (56% by mass finer than sieve #200). The as-received specimen shows no evidence of gas present. The surface texture of sediment grains is compatible with a fluvial-deltaic sedimentation environment and shows no signs of glacial entrainment. Tests conducted on sediments with and without THF hydrates show that effective stress, porosity, and hydrate saturation are the major controls on the mechanical and geophysical properties. Previously derived relationships between these variables and mechanical/geophysical parameters properly fit the measurements gathered with Mount Elbert specimens at different hydrate saturations and effective stress levels. We show that these measurements can be combined with index properties and empirical geomechanical relationships to estimate engineering design parameters. Volumetric strains measured during hydrate dissociation vanish at 2–4 MPa; therefore, minimal volumetric strains are anticipated during gas production at the Mount Elbert well. However, volume changes could increase if extensive grain crushing takes place during depressurization-driven production strategies, if the sediment has unexpectedly high in situ porosity associated to the formation history, or if fines migration and clogging cause a situation of sustained sand production.

© 2010 Elsevier Ltd. All rights reserved.

1. Introduction

Pressure and temperature constrain the formation of gas hydrates to permafrost regions and marine sediments in continental margins (Kvenvolden and Lorenson, 2001). This manuscript documents a study of hydrate-bearing sediments in permafrost. The site is about 400 km north of the Arctic Circle on the coastal plain of Alaska North Slope (Hunter et al., 2011). First, we investigate the local geology and the formation history of the permafrost and hydrate phase. Then we report results of a comprehensive experimental characterization study conducted on a single specimen recovered from the BPXA-DOE-USGS Mount Elbert Gas Hydrate Stratigraphic Test Well (Mount Elbert well): parameters include index properties, geotechnical and

geophysical characteristics obtained for the “undisturbed” sample and subsequent remolded specimens with and without THF hydrate. Finally, we explore potential implications related to gas production.

2. Hydrate and permafrost in Alaska North Slope

2.1. Site geology

The sediments at the Alaska North Slope are grouped into Franklinian, Ellesmerian and Brookian sequences in relation to tectonic episodes and lithologic characteristics (Lerand, 1973; Grantz et al., 1975). The Franklinian sequence consists of metamorphosed clastic and carbonate rocks (Reiser et al., 1978). The Ellesmerian sequence records the northward retreat of the coast line and the shallow-marine and nonmarine clastic sedimentation (Collett et al., 1988). And the Brookian sequence records a series of tectonic events: uplift of the Brook Range, subsidence of the Colville trough, and the formation of the Barrow arch caused by the

* Corresponding author. Tel.: +1 404 385 7696.

E-mail addresses: sheng.dai@gatech.edu (S. Dai), changho@gatech.edu (C. Lee), jcs@gatech.edu (J. Carlos Santamarina).

northward downwarping of the Colville trough (Grantz et al., 1979; Collett et al., 1988; Bird, 1999). Currently, the Barrow arch is approximately parallel to the present shoreline and controls the occurrence of numerous oil and gas fields including the Milne Point Unit (Grantz et al., 1975; Collett et al., 1988). Gas hydrate prospects at Milne Point Unit are found in the sand layers of the fluvial-deltaic Sagavanirktok Formation within the Brookian sequence. This complex formation includes structural compartmentalization and faults that may serve as gas migration pathways from deeper hydrocarbon reservoirs (Hennes, 2004; Casavant et al., 2004; Hunter et al., 2005).

The stratigraphy at the Mount Elbert well exhibits a stacked sequence of fluvial, deltaic and nearshore marine sands with interbedded layers of both terrestrial and marine shales (Rose et al., 2011). Gas hydrates are found in two primary horizons at the Mount Elbert well. The C unit consists of 16 meters of gas hydrate-bearing sands (depth: ~650 m to ~666 m), and the shallower D unit which consists of 14 meters of gas hydrate-bearing sands (depth: ~614 m to ~628 m). The sediment tested in this study was recovered from the D unit. Both layers have relatively high hydrate saturation ranging from $S_{\text{hyd}} = 60\text{--}75\%$; this estimate is based on analyses of well log data (Lee and Collett, 2011) and pore water geochemistry (Torres et al., 2011).

Isotopic compositional analysis shows the coexistence of thermogenic and biogenic gases at the Alaska North Slope (Collett et al., 1988; Valin and Collett, 1992; Lorenson et al., 2008). This points to two general scenarios for gas hydrate formation. One theory assumes that a pre-existing gas reservoir was converted into hydrate after favorable changes in temperature and pressure. The other suggests that gas migrated upwards into the stability zone and then formed hydrate. In particular, biogenic and/or deeper thermogenic free gases may have migrated upward through Eileen fault (Carman and Hardwick, 1983; Masterson et al., 2001; Lorenson et al., 2008). Various sealing and trapping mechanisms have been proposed, such as structured fault closures (Collett et al., 1988; Hunter et al., 2005), low permeability marine siltstone layers (Collett et al., 1988, 1990; Collett, 1993), permafrost (Pratt, 1979; Jamison et al., 1980; Downey, 1984), previously formed hydrate itself (Hunter et al., 2005), or concentrated deposits of peat or coal seams (Pratt, 1979).

2.2. Hydrate formation history

We combine various sources of information to reconstruct the evolution of the stratigraphy, ground surface, base of the ice-bearing permafrost, and potential gas hydrate stability zone at the Mount Elbert region. Data sources include: (1) logging data gathered for the Mount Elbert well, (2) stratigraphic and geologic information from the Alaska North Slope (Reimnitz et al., 1972; Bird, 1981, 1999; Collett et al., 1988; Valin and Collett, 1992; Frederiksen et al., 1998; Inks et al., 2008), and (3) information on permafrost and ground surface temperature (Wolfe, 1980; Wolfe and Upchurch, 1987; Wolfe, 1994; Brigham and Miller, 1983; Parrish et al., 1987; Spicer and Chapman, 1990; Elias and Matthews, 2002; Matheus et al., 2003; Kaufman et al., 2004; Bujak Research International, 2008). We make the following assumptions:

- Continuous permafrost starts when the mean annual ground surface temperature is lower than $-5\text{ }^{\circ}\text{C}$ (Brown, 1970). Thereafter, we place the base of the ice-bearing permafrost BIPF following Lunardini (1995) and Osterkamp and Gosink (1991).
- The temperature at the BIPF is assumed to be $-1\text{ }^{\circ}\text{C}$, based on both logging data ($-1 \pm 0.5\text{ }^{\circ}\text{C}$, Lachenbruch et al., 1982) and

salt concentration (12.7 g/L, reported later in this manuscript) which induces a $-0.8\text{ }^{\circ}\text{C}$ freezing point depression (Andersland and Ladanyi, 2004).

- The temperature within the permafrost increases with depth above the BIPF following a linear geothermal gradient of $1.64\text{ }^{\circ}\text{C}/100\text{ m}$ (Lachenbruch et al., 1982). Centennial fluctuations of the surface temperature can cause an anomalous temperature profile in the upper 160 m at Prudhoe Bay (Lachenbruch et al., 1982).
- The temperature beneath the BIPF is computed assuming that oscillations in the depth of the permafrost have a period much longer than the thermal diffusion time. Thus, we assume a time-constant, linear geothermal gradient below the permafrost ($3.56\text{ }^{\circ}\text{C}/100\text{ m}$ – from logging data in Collett et al., 2008; corroborated with data at other wells in the Alaska North Slope – refer to Lachenbruch et al., 1982; Collett et al., 1988, and Collett, 1993).
- The fluid pressure is hydrostatic and the water table is assumed at the ground surface. This assumption is based on the proximity of the Mount Elbert site to the coast line, evidence of hydrate formation before the permafrost (to be shown later in this section), and confirmatory fluid pressure data found in Collett (1993).
- The methane hydrate stability zone is computed with the pressure–temperature conditions assumed above. We use the equation by Sloan and Koh (2008) to compute the phase boundary for pure methane gas hydrate, but we modify it to fit data points generated using the HWHYD software; for temperature higher than $0\text{ }^{\circ}\text{C}$, the equation is $P\text{ [kPa]} = \exp(40.234 - 8860/T\text{ [K]})$. The effect of salt concentration on methane hydrate stability is also considered in this computation following Sloan and Koh (2008).

The computed depth–time evolution for hydrate and permafrost are summarized in Fig. 1. These results indicate that current hydrate-bearing sediments could have formed almost a million years before the onset of permafrost at Mount Elbert. The hydrate stability zone thickened as the base of the permafrost deepened. In fact, the permafrost invaded the pre-existing gas hydrate zone; therefore, ice and hydrate may coexist throughout the superposition depth. These results are compatible with hydrate formation sustained by the upwards migration of deep thermogenic gases, which became trapped together with shallower biogenic gases within the current gas hydrate stability zone and converted into hydrate as ground surface cooled in the Pleistocene epoch. Pre-existing free gas and high-conductivity faults can explain the high hydrate saturations found on the North Slope.

We can anticipate that preferential hydrate accumulation in the coarse-grained C and D units is due to either advective flow favored through the more permeable coarse-grained layers (methane transport dissolved in water), or gas invasion due to the low capillary entry pressures in coarse-grained layers with low fines content (methane transport in gas phase).

Could pore size shift pressure–temperature PT stability conditions in layers with high fines content and explain the absence of hydrate in these layers? We explore this situation taking into consideration the pressure–temperature conditions in Fig. 1. The void ratio with depth is computed using the standard 1D consolidation theory $e = e_{100} + C_c \log(\sigma'/\text{kPa})$ where e_{100} and C_c are sediment-dependent parameters (Burland, 1990). Pore size d_{pore} depends on void ratio and specific surface S_s and can be estimated as $d_{\text{pore}} = \alpha \times e/(S_s \times \rho)$ where ρ is the mineral mass density and α varies from $\alpha = 2$ for parallel face-to-face configuration to $\alpha = 6.2$ for edge-to-face aggregation of platy particles. Finally, the equilibrium temperature shift ΔT_{dep} due to pore size is computed for

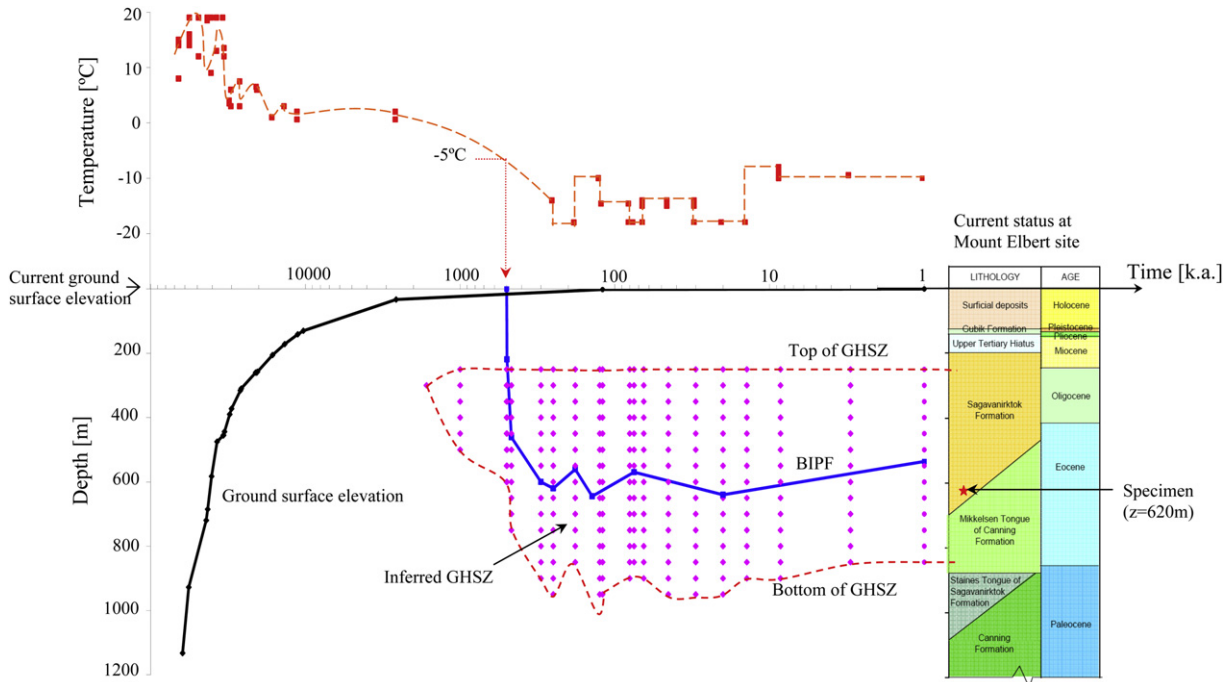


Fig. 1. Geological history at Mount Elbert site and hydrate stability zone GHSZ. Data compiled from the literature include: ground surface elevation, stratigraphy, surface temperature, and the base of the ice-bearing permafrost BIPF. The gas hydrate stability zone is computed and superimposed on the figure (assumptions and relevant expressions can be found in the text). Time is shown in logarithmic scale in unit of thousand years [k.a.].

cylindrical pores as $\Delta T_{dep} = -2\gamma_{hw}m_h T_{bulk}/d_{pore}\rho_h L_f$ (Kwon et al., 2008). Stability boundaries are shown in Fig. 2 for Mount Elbert PT conditions and for sediment parameters that correspond to silt or sand sediments (same trend as for the bulk fluid “F”), kaolin “K”, illite “I”, and montmorillonite “M”. The specific surface measured for the Mount Elbert specimen is similar to the specific surface for kaolinite; therefore, pore size had only a minor effect restricting the thickness of the hydrate stability zone.

3. Index properties and implications

The specimen studied herein was recovered from the D unit at a depth between 620.47 m and 620.62 m. This depth is below the permafrost but within the hydrate stability zone. Index properties are discussed next; a summary of all parameters is presented in Table 1.

The measured gravimetric water content $\omega_c = 26.9\%$ (oven-dried method-ASTM D2216) can be used to estimate a lower bound of the porosity $n = GS\omega_c/(1 + GS\omega_c) = 0.42$ by assuming complete water saturation. The aqueous extraction method was adopted to recover the pore fluid from the specimen (Rhoades, 1982). This extracted pore fluid has pH = 7.4 (non-bleeding type narrow range pH strips-ASTM D4972), and electrical conductivity $\sigma_{pf} = 1.9$ S/m measured at 20 °C using a Network Analyzer HP-8752A (for comparison, $\sigma_{pf} \approx 10^{-3}$ S/m in fresh water and $\sigma_{pf} \approx 4.2$ S/m in seawater at 20 °C). The total dissolved salts TDS in the pore fluid can be estimated from the measured electrical conductivity to be TDS = 12.7 g/L (empirical relationship $\sigma_{pf} = 0.15TDS$, where σ_{pf} is in mS/m and TDS in mg/L – as reported in Santamarina et al., 2001).

The grain size distribution indicates a poorly sorted silty-sand (sieve analysis-ASTM D421, and hydrometer-D422): median grain size $D_{50} = 0.07$ mm, coefficient of uniformity $C_u = 4.79$, and coefficient of curvature $C_{cur} = 1.84$. The fine fraction is 56% by mass (passes through sieve #200, i.e $d < 75 \mu m$). The specific surface is $11.3 \text{ m}^2/\text{g}$ (methylene blue method – value in the range of kaolinite

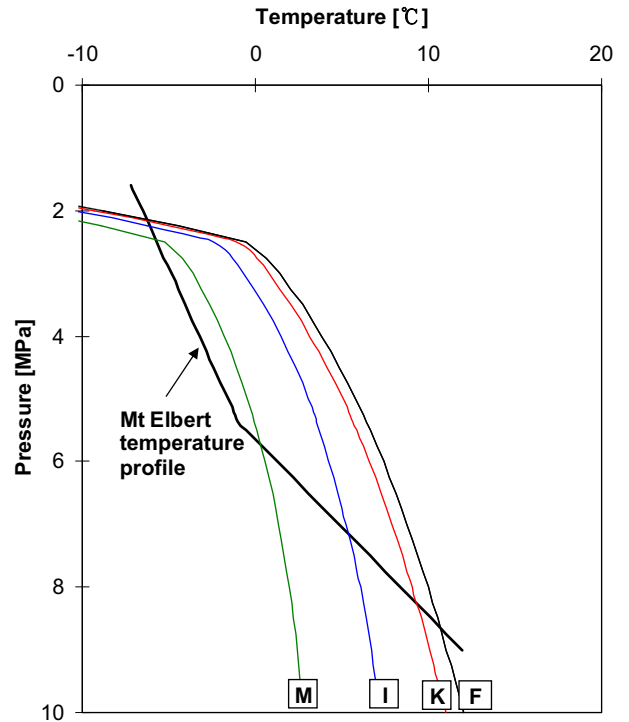


Fig. 2. Pore size-dependent shift in the phase boundary and in situ pressure and temperature profile at the Mount Elbert site. Trends computed for silt and sands (same trend as for the bulk fluid “F”), kaolin “K” ($e_{100} = 0.89$, $C_c = 0.29$, $S_s = 10 \text{ m}^2/\text{g}$), illite “I” ($e_{100} = 2.05$, $C_c = 0.82$, $S_s = 70 \text{ m}^2/\text{g}$), and montmorillonite “M” ($e_{100} = 3.06$, $C_c = 1.15$, $S_s = 300 \text{ m}^2/\text{g}$). In terms of specific surface, the tested specimen corresponds to “K”; therefore, pore size had only a minor effect restricting the thickness of the hydrate stability zone.

Table 1
Index and engineering properties of Mount Elbert sediment (specimen from depth $z = 620.47\text{--}620.62$ m).

Index properties	This study		Other depths ^a	
	Values	Device/Technique		
			¹ Z = 619.47–619.49 m; ² Z = 620.32–620.46 m; ³ Z = 623.16–623.23 m; ⁴ Z = 623.56–623.58 m	
Median diameter D_{50}	0.07 mm	Sieve and hydrometer	¹ 0.074; ³ 0.061	
Coefficient of uniformity C_u	4.8	(ASTM D421, D422)	¹ 10; ³ 20.56	
Coefficient of curvature C_{cur}	1.8		¹ 2.68; ³ 2.11	
Passing sieve #200	56%		¹ 50%; ³ 61%	
Roundness R	0.47	Leica MZ6 stereomicroscope		
Sphericity S	0.62	(Krumbein and Sloss, 1963; Santamarina et al., 2001)		
Specific surface S_s	11.3 m ² /g	Methylene blue (Santamarina et al., 2002)		
Specific gravity G_s	2.67	Pycnometer (ASTM D854)		
Maximum void ratio e_{max}	1.10	ASTM D4254		
	1.01–1.07 ^b			
Composition/mineralogy	Si = 61% Ta = 12% Al = 12% O = 10% K = 1.5% Mg = 1.0% Other = 2.3%	Hitachi S-3500 SEM, EDX	² Quartz = 83% Plagioclase = 4% Pyrite = 2% K-spar = 1% Chlorite = 3% Kaolinite = 2% Illite = 3%	⁴ Quartz = 81% Plagioclase = 7% Pyrite = 1% K-spar = 1% Chlorite = 3% Kaolinite = 2% Illite = 3%
Porosity n	0.42 (as received)		¹ 42.6; ³ 43	
Initial void ratio e_0	0.72 (as received)		¹ 0.74; ³ 0.75	
pH	7.4	Non-bleeding pH strip (ASTM D4972, Rhoades, 1982)		
Electrical conductivity of pore fluid σ_{pf}	1.9 S/m	High frequency network analyzer at 1 GHz (HP-8752A)		
Total dissolved salts in pore fluid	12.7 g/L	Computed from σ_{pf}		
<i>Engineering properties (no hydrate)</i>				
Compression index C_c	0.07	Oedometer	–	
Swelling index C_s	0.006		–	
V_s at 1 kPa means stress: α	35.36	Bender element in oedometer cell		
Sensitivity of V_s to σ'_v : β	0.295			
Constant volume friction angle ϕ_{cv}	$35^\circ \pm 2^\circ$ ^c 34° ^{a,b}			
Permeability	$1.2\text{--}3.5 \times 10^5$ md	Computed from Hazen's equation based on D_{10}	² 2100 md (to air at 4.03 MPa) ⁴ 1370 md (to air at 4.03 MPa)	

^a Winters et al. (2011).

^b Estimated using relations in Cho et al. (2006).

^c Simplified procedure in Santamarina and Cho (2001).

clay). The high fraction of fine particles and relatively high specific surface hinder fluid conduction and hydrate accumulation, and affect the sediment stiffness and strength.

Compositional EDX (Energy-dispersive X-ray spectroscopy) analysis shows that silicon (61.3%), tantalum (12.3%), aluminum (11.9%), and oxygen (9.7%) are the major components. This composition is roughly consistent with the reported mineralogy: quartz = 81–83%, plagioclase = 4–7%, pyrite = 1–2%, K-spar = 1%, chlorite = 3%, kaolinite = 2%, and illite = 3% (Winters et al., 2011 – details in Table 1). Composition and mineralogy are in agreement with the measured value of specific gravity $G_s = 2.67$ (pycnometer, ASTM D854).

Particle size, shape, and surface texture reflect grain composition and formation history, and determine the sediment mechanical behavior. The grain surface texture was observed using a scanning electron microscope (Hitachi S-3500). Representative grain surface textures are shown in Fig. 3. Most grains have medium to high relief, abrupt edges, and v-shaped percussions that suggest intensive collisions and crushing. V-shaped percussion fractures are also present in glacial grains, especially when grains are emplaced by fast moving wet-based glaciers; however, dominant microtextures obtained in glacial grains are missing in these sediments, in particular there is no evidence of subparallel grooves, conchoidal fractures, edge rounding, linear and curved troughs, and

multiple adhering particles (Krinsley and Doornkamp, 1973; Mahaney and Kalm, 1996; Mahaney, 2002). Sphericity S and roundness R were visually determined using a stereomicroscope (Leica MZ6- chart in Krumbein and Sloss, 1963); mean values are $S = 0.62$ and $R = 0.47$. We can conclude on the bases of observed and missing features that the tested specimen agrees with the fluvial-deltaic origin of gas hydrate-bearing sediments at Mount Elbert, and have not experienced glacial entrainment.

The loosest packing density was obtained by funneling dry sediment to obtain the maximum void ratio $e_{max} = 1.10$ and porosity $n_{max} = 0.52$ (ASTM D4254). Particle shape data are used to obtain a second estimation of the maximum void ratio $e_{max} = 1.01\text{--}1.07$ which is roughly in agreement with the measured value. The shape-based estimate of the minimum void ratio $e_{min} = 0.64\text{--}0.68$ could not be experimentally confirmed due to the limited amount of sediments (Cho et al., 2006).

Large strain shear strength involves particle rotation and contact slippage, which are affected by particle shape. Published correlations and measured grain shape parameters S and R allow us to estimate the constant volume friction angle as $\phi_{cv} = 34^\circ$ (data in Table 1 – Cho et al., 2006); this angle approximately agrees with the value measured using the angle of repose method $\phi_{cv} = 35^\circ \pm 2^\circ$ (simplified procedure in Santamarina and Cho, 2001).

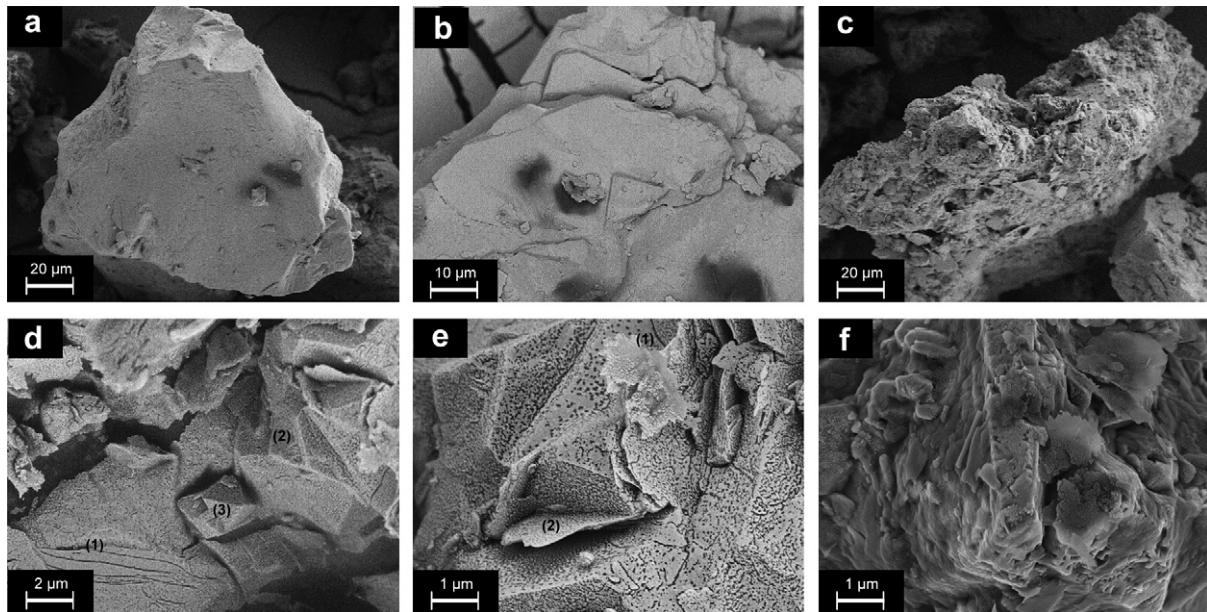


Fig. 3. Grain surface texture (note: scales are not uniform). (a, b) High relief, abrupt angular features and fine cracks indicate on going crushing. (c) Craters and cavities associated to chemical weathering. (d) Fine subparallel (1), sharp (2) fractures, and well abraded stylus of possibly heavy minerals (3) (Mahaney, 2002). (e) Crack (1), sharp cut (2) and overwhelmed v-shape percussions on the surface of the grain indicate intensive collision (Krinsley and Doornkamp, 1973; Mahaney, 2002). (f) Precipitation, the sharp features of the original broken face in the lower left of the micrograph has been dulled by precipitation.

4. Core characterization – structure of the as-received sediment

The core was sealed and frozen as soon as it was recovered from the Mount Elbert test well (diameter ~70 mm, length 80 mm). The sample arrived at our laboratory in a frozen state at standard pressure (1 atm). While depressurization and freezing alter the fabric, the as-received state still captures meso-scale features that are lost after thawing and remolding.

The specimen was gradually covered by a protective wax layer without causing thawing. By using standard gravimetric and volumetric measurements, we obtained the initial void ratio of the specimen $e_0 = 0.72$ (ASTM D2216), which corresponds to an initial porosity $n_0 = 0.42$, in agreement with the lower bound estimate based on water content.

4.1. Spatial variability

We used two methods to assess the spatial variability of the core: X-ray images (frozen state – Dage XD7600NT) and the electrical needle probe technique (thawed specimen within the wax shell – Cho et al., 2004).

The color variation in the X-ray image (see 2D slice in Fig. 4a) and oscillations in electrical resistance profiles (Fig. 4b) represent variance in sediment porosity and/or composition. Both resistance profiles and X-ray images show relatively lower porosity in the upper and lower zones than in the center of this specimen. There is no clear evidence of pre-existing hydrate lenses in the X-ray image as fluids migrated after depressurization; only faint traces of discontinuities remain (see arrows in Fig. 4a).

4.2. Evolution of seismic wave velocities during initial thaw

Frozen pore fluid has minimal effect on X-ray absorption in soils, but a pronounced effect on acoustic velocities and electrical properties (Lee et al., 2007). Therefore, we monitored the evolution of temperature, P-wave and S-wave velocities during the first thawing of the as-received specimen. Results plotted in Fig. 5 highlight the

great impact frozen fluids exert on the stiffness of sediments without external stress: propagation velocities in the frozen sediment are $V_p = 2550$ m/s and $V_s = 734$ m/s and fall to $V_p = 1500$ m/s and $V_s = 50$ m/s after complete thawing (Note: the velocity of sound in degassed water is $V_p \approx 1480$ m/s, and it experiences a pronounced decrease in the presence of gas, e.g., a 35% decrease in V_p is observed for a volume fraction of gas as low as 10^{-4}). Wave velocities measured after thawing the specimen indicate that this sediment is fully water saturated and not-cemented. Complete water saturation could imply that this specimen did not contain hydrate in situ.

The measured P-wave and S-wave velocities are length-averaged values and integrate the travel time through frozen and thawed regions. We invert for the “remnant frozen length” using the travel times for both P and S propagations and the velocities for the frozen condition ($V_p = 2550$ m/s and $V_s = 734$ m/s) and the unfrozen state ($V_p = 1500$ m/s and $V_s = 50$ m/s). Results in Fig. 5d show that the frozen length shortens while the temperature measured at the center of the core remains constant at the water-ice phase boundary. The end of thawing, i.e., when the inferred frozen length reaches zero, coincides with the increase in the core temperature above zero degrees. These results show that the complementary use of P- and S-wave propagation provides insightful information that can be used to characterize and delineate permafrost sediments and to monitor thawing or dissociation such as during gas production from hydrate-bearing sediments. We have applied similar techniques to monitor the depressurization of pressure cores gathered from hydrate-bearing sediments in the Krishna–Godavari basin (India) and the Ulleung basin (East Sea); high attenuation hinders P-wave propagation soon after dissociation starts and free gas emerges.

5. Geophysical properties and stress–volume response (remolded sediment)

The stress–volume response was studied using an instrumented oedometer cell which houses shear wave transducers, a dielectric probe for complex permittivity measurement, and a K-type

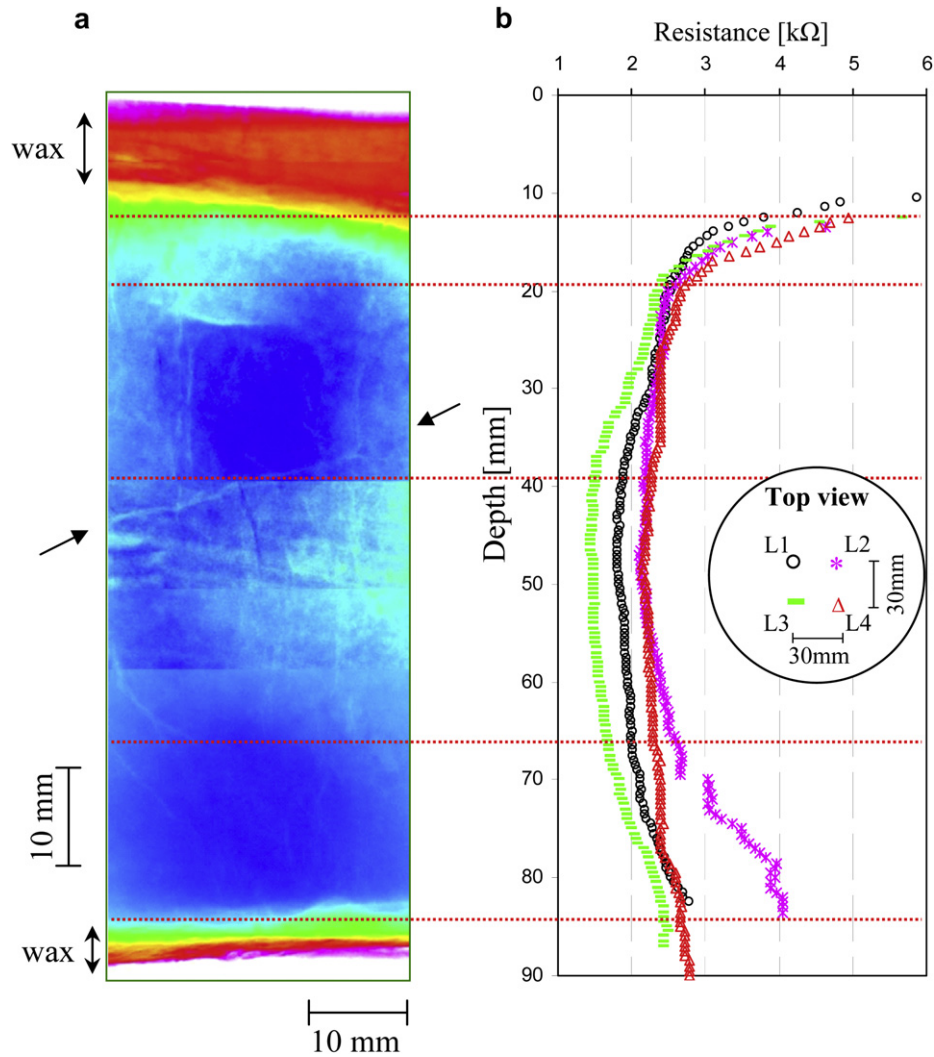


Fig. 4. Spatial variability characterization of undisturbed sediment. (a) X-ray image taken for the as-received frozen sediment – only the longitudinal central band is shown to highlight features without edge effects. (b) Longitudinal electrical resistance profiles gathered at four locations after thawing the sediment.

thermocouple. The remolded sediment was mixed with three different pore fluids: (1) deionized water, (2) a 57:43 THF-water solution to obtain 50% hydrate saturation $S_{\text{hyd}} = 0.5$ with excess THF to avoid freezing, and (3) a 19:81 THF-water solution to reach $S_{\text{hyd}} = 1.0$ after phase transformation. Standard consolidation test procedures (ASTM D2435) were followed for the specimen mixed with deionized water, while hydrate formation and dissociation stages were imposed after each consolidation step in specimens mixed with THF solutions. Additional details can be found in similar studies by Yun et al. (2007) and Lee et al. (2008); a detailed discussion on the use of THF as hydrate former is presented in Lee et al. (2007).

5.1. S-wave velocity

A selection of S-wave signatures is presented in Fig. 6. Signatures gathered for the specimen without hydrate at the end of each consolidation step (Fig. 6a) show that the S-wave velocity increases with the increase in effective stress, demonstrating the critical role of effective stress on the stiffness of uncemented sediments. The impact of hydrate formation and dissociation on the stiffness of hydrate-bearing sediments under a certain effective stress is

highlighted by signatures in Fig. 6b and 6c where hydrate formation leads to a pronounced increase in S-wave velocity.

Shear wave velocities for sediments with and without hydrate are shown in Figs. 7b, 8b, and 9b. Results confirm that shear wave velocity is controlled by vertical effective stress in sediments without hydrate (Fig. 7b). When a Hertzian-type model is employed, the vertically propagating shear wave velocity in uncemented sediments loaded under zero-lateral strain condition can be expressed as:

$$V_s = \alpha \left(\frac{\sigma'_v}{\text{kPa}} \right)^\beta \quad (1)$$

where, the α -factor denotes V_s at 1 kPa vertical effective stress, and the β -exponent captures the sensitivity of shear wave velocity to effective stress. Experimental observations indicate that α and β parameters depend on packing, fabric, and the type of intergranular contacts (for detailed information, refer to Santamarina et al., 2001). For this Mount Elbert sediment, the fitted values $\alpha = 40.8$ m/s and $\beta = 0.25$ ($r^2 = 0.94$) point to a sediment stiffness of high sensitivity to the stress state. The shear wave velocity for the sediment with hydrate saturation $S_{\text{hyd}} = 0.5$ combines both stress and cementation effects on stiffness (Fig. 8b). Finally, the sediment

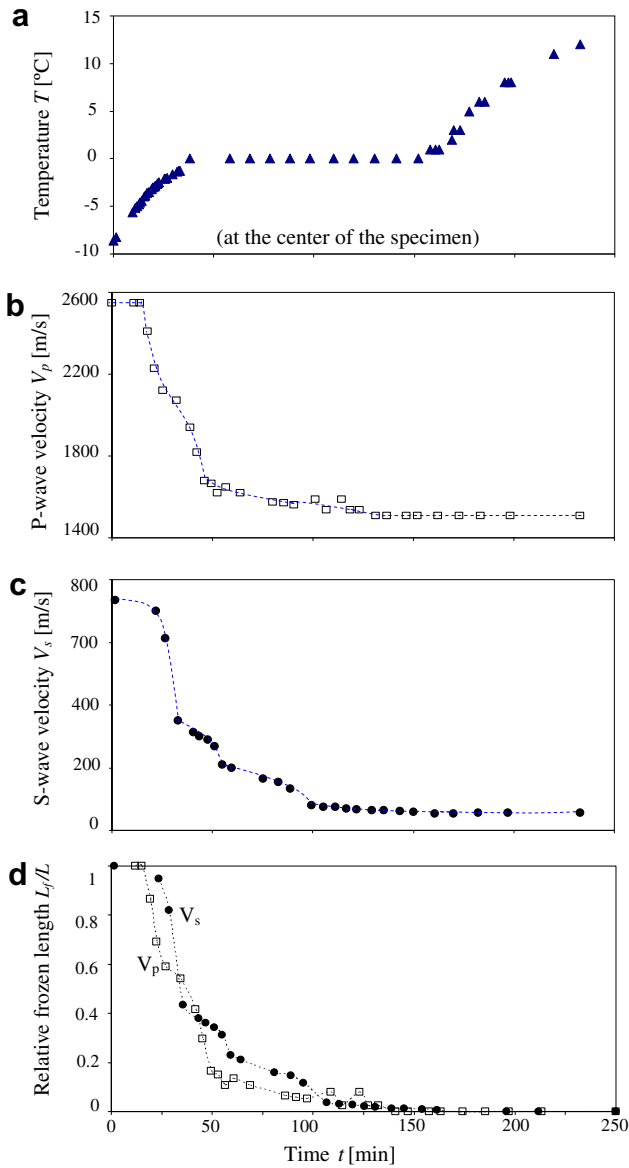


Fig. 5. Evolution of geophysical parameters during thawing of the as-received frozen sediment. (a) Temperature. (b) P-wave velocity. (c) S-wave velocity. (d) Inferred frozen sediment length L_f with respect to time during thawing; both P- and S-wave velocities are used to invert for L_f .

with 100% hydrate pore saturation $S_{\text{hyd}} = 1.0$, exhibits a stress-independent that ranges from $V_s = 1520\text{--}1580$ m/s (Fig. 9b). Note that the propagation velocity in the as-received frozen specimen was only $V_s = 734$ m/s, suggesting sampling effects.

5.2. Dielectric permittivity

Permittivity spectra in the microwave frequency range for different types of mixtures are shown in Fig. 10 (gathered using HP-8752A analyzer and dielectric probe). These spectra highlight the governing role of free water orientational polarization, the decrease in real permittivity κ in solutions with THF and in low porosity soil mixtures (Santamarina et al., 2001). The decrease in real permittivity with the increase in effective stress acting on the mixture prepared with deionized water is caused by the decrease in volumetric water fraction during sediment compaction (Fig. 7c). On the other hand, the decrease in permittivity during hydrate formations

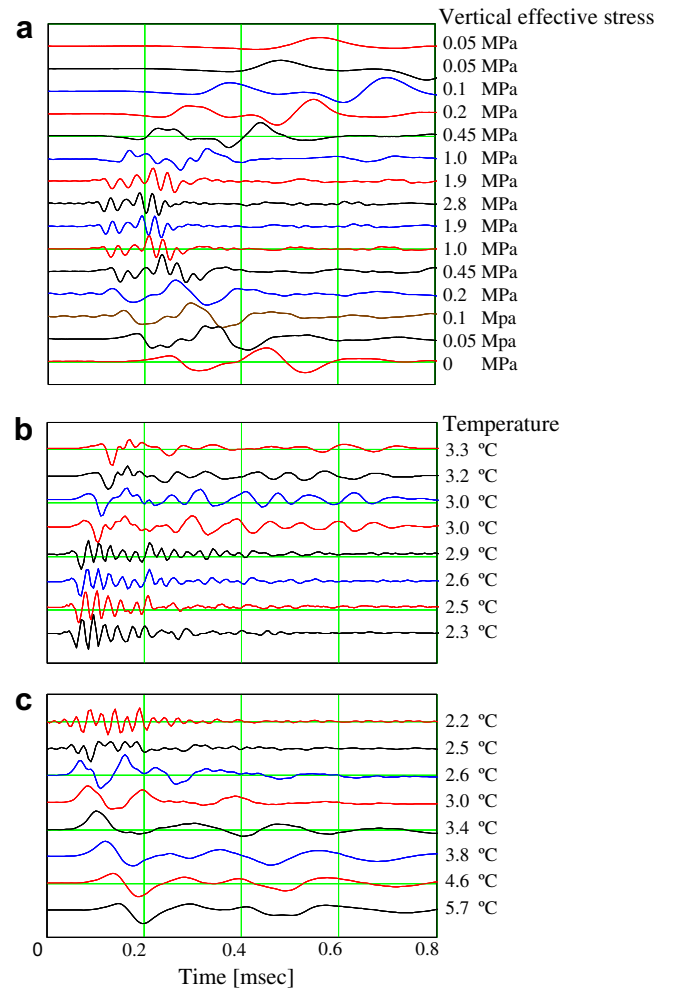


Fig. 6. Evolution of S-wave signatures gathered for the specimen saturated with 19THF:81H₂O. (a) Without hydrate at the end of each loading and unloading step. (b) During hydrate formation to reach $S_{\text{hyd}} = 1.0$ ($\sigma'_v = 0.45$ MPa). (c) During hydrate dissociation (at constant vertical stress $\sigma'_v = 1$ MPa).

reflects the decrease in polarizability as water molecules become part of hydrate cages (see data in Fig. 9c for the sediment mixed with 19:81 THF-water solution).

5.3. Electrical conductivity

The pore fluid electrical conductivity σ_{pf} is a measure of ionic concentration and mobility. The sediment electrical conductivity σ_{el} is determined by the pore fluid conductivity and the fluid-filled porosity $n(1 - S_{\text{hyd}})$. The common role of porosity in permittivity and conductivity explains the similar trends measured for electrical conductivity and permittivity (Figs. 7d and 9d). These results imply that dielectric permittivity and electrical conductivity are effective indicators of hydrate presence in sediments (note: electrical parameters for the sediment with 57:43 THF-water solution are not shown since an excess THF mixture is used). However, permittivity is primarily affected by water content while conductivity is also affected by ionic concentration and mobility.

5.4. Volume change

The change in void ratio e with effective stress σ'_v is documented in Figs. 7a, 8a and 9a for the three mixtures. Trends are very similar

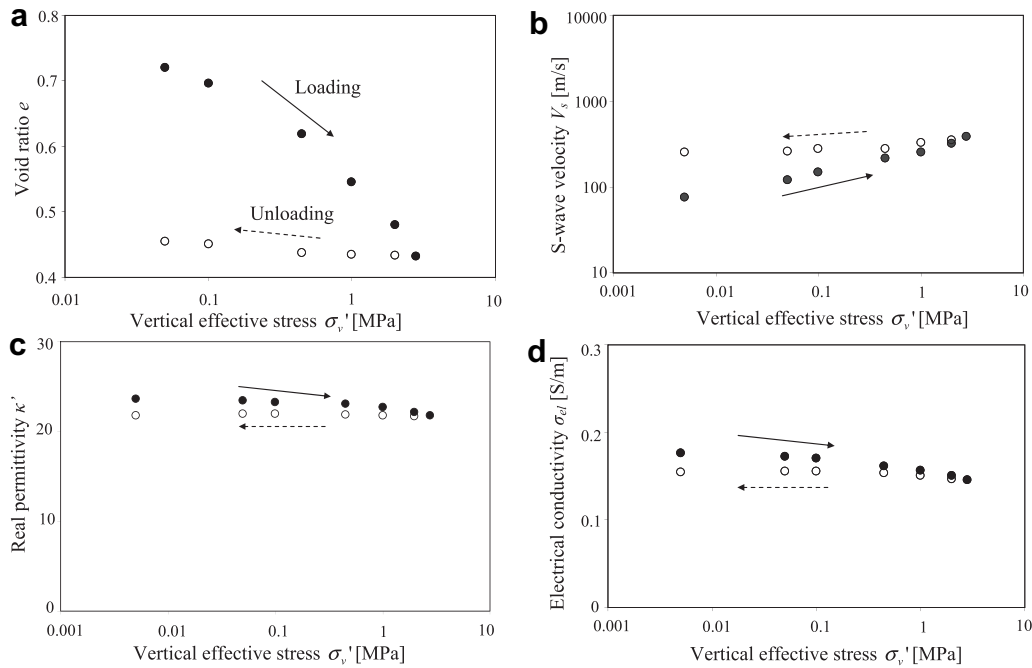


Fig. 7. Mount Elbert sediment mixed with 100% water during loading and unloading: Evolution of void ratio e , shear wave velocity V_s , real permittivity κ' , and electrical conductivity σ_{et} .

for these mixtures. Compression C_c and swelling C_s indices characterize the mechanical responses in terms of the slopes of the normal consolidation line and the unloading curve on a plot of void ratio vs. the logarithm of vertical effective stress σ'_v . The sediment can be modeled using $C_c=0.07$ and $C_s=0.006$; these values correspond to sediments with low compression and expansion properties.

The mixtures with $S_{hyd}=0.5$ and $S_{hyd}=1.0$ experience volume change during hydrate formation and dissociation. Changes appear small in Figs. 8a and 9a; data are plotted again in Fig. 11 but in terms of strain $\epsilon_z = \Delta H/H_0$, where ΔH is the change in specimen height during phase transformation and H_0 is the specimen height at the beginning of the hydrate formation or dissociation phase. Results in Fig. 11 clearly show (1) expansion during formation and contraction during dissociation, (2) diminishing volume change with increasing confinement, and (3) slightly higher contraction than expansion; hence, there is residual volume contraction after a formation-dissociation cycle. The last observation suggests that volume expansion during hydrate formation alters the stability of granular

columns and leads to skeletal collapse during hydrate dissociation (Lee et al., 2009).

Fig. 1 shows that some sedimentation continued after hydrate formation started about 1.65 Ma before present. As hydrate could have prevented sediment compaction, higher volumetric strain could take place in these layers during hydrate dissociation.

6. Analysis and discussion

Experimental results demonstrate that vertical effective stress, porosity, and hydrate saturation are the major controls on the mechanical and geophysical response of hydrate-bearing sediment. Interrelationships among these parameters are explored next. Results obtained in this study are compared with the database of geophysical parameters gathered for hydrate-bearing sediments at Georgia Tech, and semiempirical equations in Santamarina and Ruppel (2010).

Permittivity: permittivity values κ at 1 GHz are plotted as a function of porosity and hydrate saturation in Fig. 12a. We

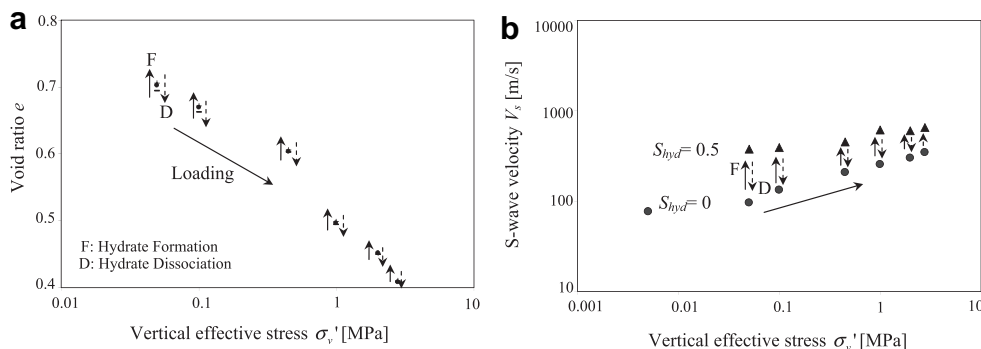


Fig. 8. Mount Elbert sediment saturated with 57THF:43H₂O pore fluid: Evolution of void ratio e and shear wave velocity V_s during loading and hydrate formation ($S_{hyd}=0.5$) and dissociation. Electrical parameters not shown because excess THF mixture is used.

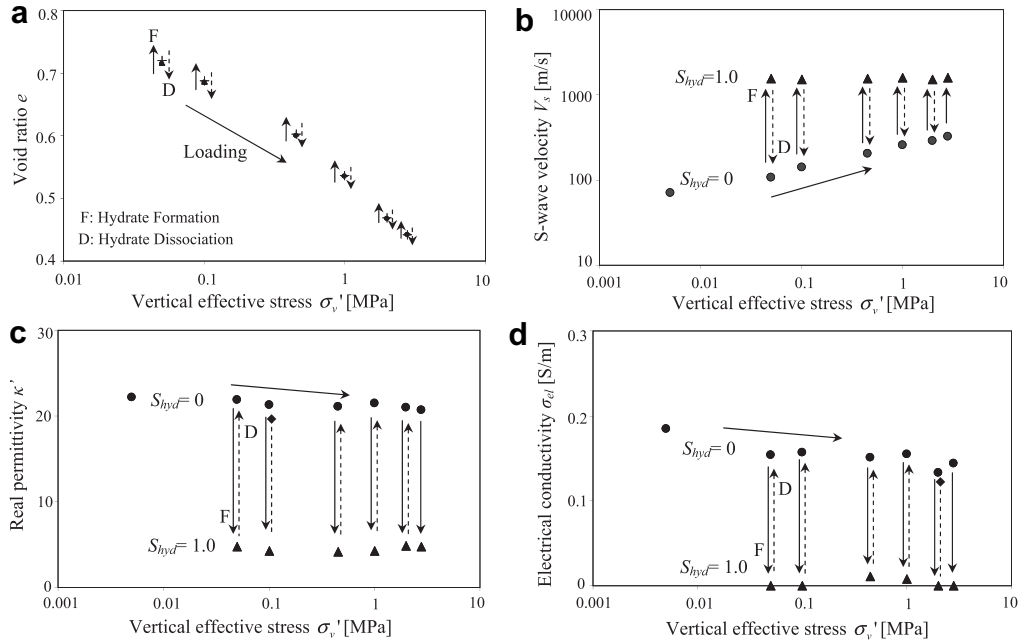


Fig. 9. Mount Elbert sediment with 19THF:81H₂O pore fluid: Evolution of void ratio e , shear wave velocity V_s , real permittivity κ' , and electrical conductivity σ_{el} during loading, hydrate formation ($S_{hyd} = 1.0$) and dissociation. The interpretation of electrical parameters κ' and σ_{el} for the unfrozen sediment must take into consideration the presence of THF in the pore fluid (refer to Fig. 6).

recognize the prevalent role of free water on permittivity and use a robust Complex Refractive Index Method CRIM model to fit the data:

$$\sqrt{\kappa} \approx 2.8 + 6n - 7nS_{hyd} \quad (2)$$

Conductivity: the ratio σ_{el}/σ_{pf} between the measured sediment conductivity σ_{el} and the pore fluid conductivity σ_{pf} , is plotted in Fig. 12b as a function of porosity and hydrate saturation. A simple form of Archie's Law fits the data:

$$\sigma_{el}/\sigma_{pf} = [n(1 - S_{hyd})]^{1.45} \quad (3)$$

S-wave velocity: the complete S-wave velocity data set for different hydrate saturations ($S_{hyd} = 0, 0.5, \text{ and } 1.0$) and vertical effective stress levels is summarized in Fig. 12c. Trends clearly show the transition from stress-controlled to hydrate-controlled stiffness

in hydrate-bearing sediments. We fit the data using a theoretical expression initially developed for cemented soils (Fernandez and Santamarina, 2001):

$$V_{hbs} = \sqrt{\left(\frac{V_h S_{hyd}^2}{n}\right)^2 \theta + \left[\alpha \left(\frac{\sigma'_{||} + \sigma'_{\perp}}{2 \text{ kPa}}\right)^\beta\right]^2} \quad (4)$$

where, $\alpha = 40.8$ and $\beta = 0.25$ correspond to the sediment without hydrate (Fig. 7b), and the fitted parameter $\theta = 0.38$ reflects the hydrate habit in pores (Santamarina and Ruppel, 2010). While a quantitative interpretation of the factor θ is not yet available, we can advance that $\theta = 0$ for pore filling hydrate and may exceed $\theta = 1.0$ for cementing hydrate.

Sand crushing: the oedometer cell used in this study is limited to a maximum vertical stress of $\sigma'_v = 2.8$ MPa. Surface features noted in

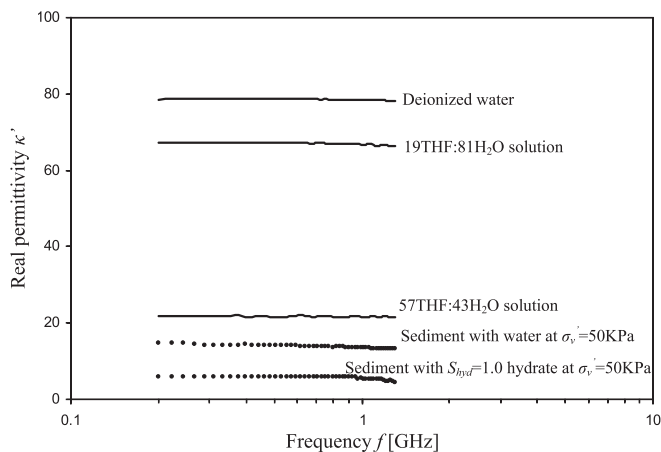


Fig. 10. Real permittivity spectra. Data shown for water, THF solutions, and sediment with and without hydrate.

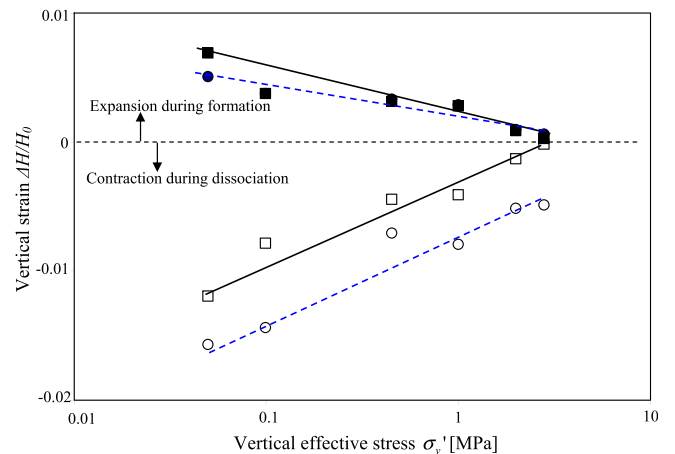


Fig. 11. Vertical strain for sediments mixed with 57THF:43H₂O pore fluid (circles) and 19THF:81H₂O pore fluid (squares) during hydrate formation and dissociation. H_0 is the height of sediment at the beginning of each formation or dissociation state.

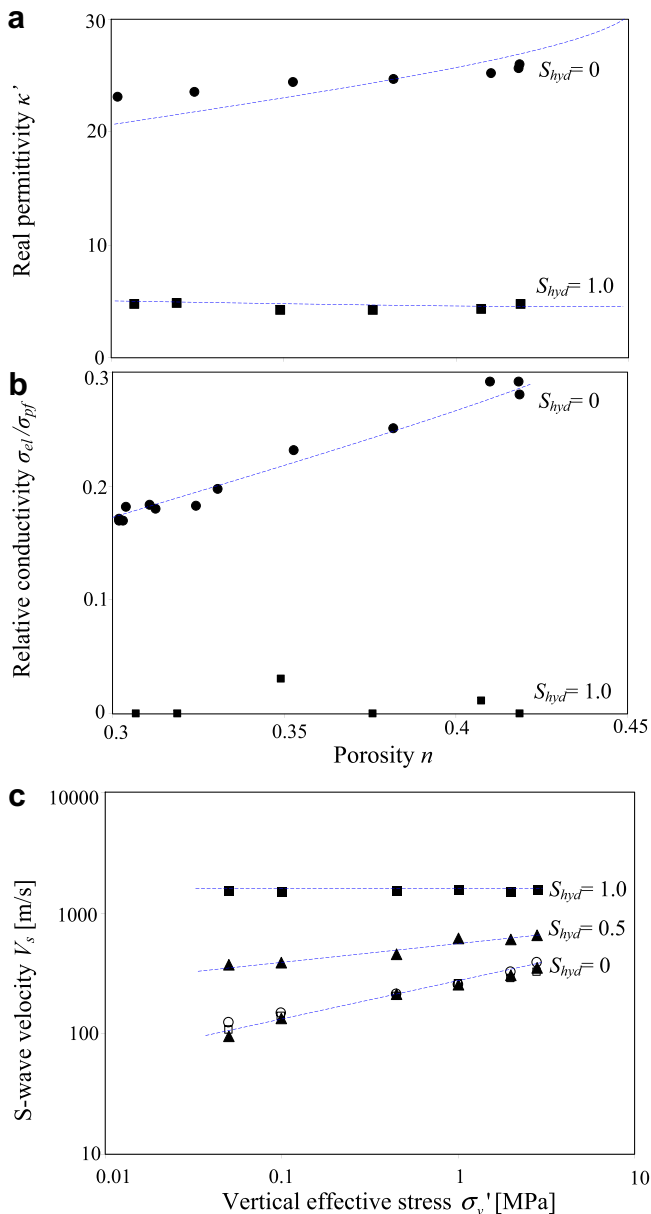


Fig. 12. Data summary: (a, b) Permittivity and conductivity as a function of porosity and hydrate saturation. (c) S-wave velocity as a function of vertical effective stress σ_v' and hydrate saturation S_{hyd} . Symbols are data points. Lines correspond to fitted models.

Fig. 3 may be related to the high effective stress in situ (6–7 MPa): for a median particle size $D_{50} = 0.07$ mm and initial void ratio $e_0 = 0.72$, the vertical yield stress at massive grain crushing is estimated to be $\sigma_y \approx 10$ –20 MPa for a 100% quartz sand, yet, some crushing starts at stress levels as low as ~ 4 MPa (Lo and Roy, 1973; Yamamuro and Lade, 1996; McDowell, 1999; Nakata et al., 2001). Thus, depressurization-driven gas production from deep hydrate-bearing sediments may cause contraction due to sand crushing, in addition to contraction due to hydrate dissociation reported in Fig. 11.

Fines migration and clogging: fines in the sediment and crushing-generated fines may migrate during gas production. Fines migration is controlled by particle size, the ratio of migrating particle size to pore constriction size, and the spatial variability of the flow velocity field. Experimental results show annular clogging in radial flow when the orifice-to-particle size ratio is smaller than

$d_{or}/d_p < 3$ –4 and when seepage velocities exceed threshold values (detailed information and data for single-phase flow can be found in Valdes and Santamarina, 2006, 2007). We estimate that the Mount Elbert sediment tested in this study is prone to fines migration and clogging. Proper gas production strategies will be needed to prevent formation damage which may also cause sustained sand production.

7. Conclusions

The analysis of published investigations and a systematic laboratory study conducted using undisturbed and remolded specimens from the Mount Elbert well reveal the following observations (note: experimental results presented in this study are based on a single specimen; significant variations should be expected along the sediment column):

- The reconstructed stratigraphy, historical ground surface elevation, base of the ice-bearing permafrost, and potential gas hydrate stability zone at the Mount Elbert region suggest that gas invaded/accumulated in coarse-grained layers and converted into hydrate-bearing sediments almost a million years before the permafrost. Any remaining water froze when the permafrost thickened and invaded the hydrate stability zone. Hence ice and hydrate may coexist at certain depths.
- Gas invasion and accumulation in coarse-grained layers before pressure–temperature stability conditions help explain the relatively high hydrate saturation found in coarse-grained layers at the Mount Elbert well. High fines content in other layers hindered fluid flow, methane transport and hydrate accumulation. The pore size-dependent shift in the *PT* phase boundary is not sufficient to impede hydrate formation in these sediments.
- Grain surface texture features are consistent with the previously suggested fluvial-deltaic origin of these sediments, without glacial entrainment. The effective stress level corresponds to the onset of crushing. S-wave velocity during the initial thawing of the as-received sediment indicates unconsolidated granular skeleton. The tested specimen has a high fraction of fines and shows no evidence of hydrate present.
- The volumetric strain during dissociation vanishes when the effective stress exceeds 2–4 MPa. Therefore, small volumetric strains are expected during gas production at the Mount Elbert well, where the in situ stress exceeds 6–7 MPa. Two possible situations may alter this conclusion: (1) crushing associated to the increase in effective stress during depressurization-driven production, and (2) high in situ porosity if early hydrate formation prevented densification. Grain crushing may feed fines migration and clogging, which in turn could contribute destabilization and sustained sand production.
- The major controls on the mechanical and geophysical properties of hydrate-bearing sediments are effective stress, porosity, and hydrate saturation. Geophysical parameters and established empirical relationships in geomechanics allow us to obtain robust estimates of engineering design parameters for hydrate-bearing sediments. Furthermore, elastic and electromagnetic wave measurements can be employed to characterize and delineate hydrate-bearing/permafrost sediments and to monitor dissociation/thawing processes, during gas production from hydrate-bearing sediments.

Acknowledgements

Support for this research was provided by the Joint Industry Project for Methane Hydrate, administered by Chevron, and by the

Gas-Production Project, both funded by DOE's National Energy Technology Laboratory. Additional support was provided by the Goizueta Foundation. Ray Boswell, Kelly Rose and Eilis Rosenbaum provided the specimen.

References

- Andersland, O.B., Ladanyi, B., 2004. In: *Frozen Ground Engineering*, second ed. John Wiley & Sons, Inc.
- Bird, K.J., 1981. Machine-generated displays of well logs and lithology from selected wells on the North Slope of Alaska; 7 wells from the east-central North Slope. U.S. Geological Survey Open-File Report 81-1036.
- Bird, K.J., 1999. Geographic and geologic setting. Chapter GG, In: *The Oil and Gas Resource Potential of the Arctic National Wildlife Refuge 1002 Area, Alaska*, by ANWR Assessment Team: U.S. Geological Survey Open-File Report 98-34.
- Brigham, K.K., Miller, G.H., 1983. Paleotemperature estimates of the Alaskan Arctic Coastal Plain during the last 125,000 years. In: *Proceedings of Fourth International Conference on Permafrost, 17–22 July, Fairbanks, Alaska*. Washington, D.C. National Academy Press, pp. 80–85.
- Brown, R.J.E., 1970. Permafrost in Canada. University of Toronto Press, Toronto, 234 pp.
- Bujak Research International., 2008. *Palynological Biostratigraphy of the Interval 1990–2484ft Mount Elbert 01 Well Northern Alaska*. Report, 23 pp.
- Burland, J.B., 1990. On the compressibility and shear strength of natural clays. *Geotechnique* 40 (3), 329–378.
- Carman, G.J., Hardwick, P., 1983. Geology and regional setting of Kuparuk Oil Field, Alaska. *American Association of Petroleum Geologists Bulletin* 67 (6), 1014–1031.
- Casavant, R., Hennes, A., Johnson, R., Collett, T., 2004. Structural analysis of a proposed pull-apart basin: Implications for gas hydrate and associated free-gas emplacement, Milne Point Unit, Arctic Alaska, Vancouver, BC, Canada. The American Association of Petroleum Geologists Hedberg Research Conference. September, 12–16.
- Cho, G.C., Lee, J.S., Santamarina, J.C., 2004. Spatial variability in soils: high resolution assessment with electrical needle probe. *ASCE Journal Geotechnical and Geoenvironmental Engineering* 130 (8), 843–850.
- Cho, G.C., Dodds, J.S., Santamarina, J.C., 2006. Particle Shape effects on packing density, stiffness and strength – natural and crushed sands. *ASCE Journal Geotechnical and Geoenvironmental Engineering* 132 (5), 591–602.
- Collett, T.S., Bird, K.J., Kvenvolden, K.A., Magoon, L.B., 1988. Geologic interrelations relative to gas hydrates within the North Slope of Alaska. *USGS Open-File Report* 88-389.
- Collett, T.S., Bird, K.J., Kvenvolden, K.A., Lee, M.W., 1990. Terrestrial gas hydrate occurrences. *Proc. Nat. Gas. R.D. Contr. Rev. Meeting, DOE/METC-91/6117*, pp. 205–214.
- Collett, T.S., et al., 2008. Energy source potential of gas hydrates on the North Slope of Alaska-Project briefing. BP-DOE Gas Hydrate Meeting presentation on March 08, Personal communication.
- Collett, T.S., 1993. Natural gas hydrate of Prudhoe Bay and Kuparuk River area, North Slope, Alaska. *AAPG Bulletin* 77 (5), 793–812.
- Downey, M.W., 1984. Evaluating seals for hydrocarbon accumulations. *AAPG Bulletin* 68 (11), 1752–1763.
- Elias, S.A., Matthews Jr., J.V., 2002. Arctic North American seasonal temperatures from latest Miocene to the Early Pleistocene, based on mutual climatic range analysis of fossil beetle assemblages. *Canadian Journal Earth Science* 39, 911–920.
- Fernandez, A., Santamarina, J.C., 2001. The effect of cementation on the small strain parameters of sands. *Canadian Geotechnical Journal* 38 (1), 191–199.
- Frederiksen, N.O., Andrieu, V.A., Sheehan, T.P., Ager, T.A., Collett, T.S., Fouch, T.D., Franczyk, K.J., Johnson M.J., 1998. Palynological dating of Upper Cretaceous to middle Eocene strata in the Sagavanirktok and Canning formations, North Slope of Alaska. U.S. Geological Survey Open-File Report 98-471.
- Grantz, A., Holmes, M.L., Kososki, B.A., 1975. Geologic framework of the Alaskan continental terrace in the Chukchi and Beaufort Sea. In: *Yorath, Parker, Glass (Eds.), Canada's Continental Margins and Offshore Petroleum Exploration*. Canadian Society of Petroleum Geologists Memoir 4, 669–700.
- Grantz, A., Eitrem, S., Dinter, D.A., 1979. Geology and tectonic development of the continental margin north of Alaska. *Tectonophysics* 59, 263–291.
- Hennes, A., 2004. Structural constraints on gas-hydrate formation and distribution in the Milne Point, North Slope of Alaska. M.S. thesis, Department of Geosciences, University of Arizona.
- Hunter, R., Patil, S., Casavant, R., Collett, T., 2005. Resource characterization and quantification of natural gas-hydrate and associated free-gas accumulations in the Prudhoe Bay – Kuparuk River Area on the North Slope of Alaska. DE-FC-01NT41332 quarterly report 8-9 of U.S. DOE/NETL.
- Hunter, R.B., Collett, T.S., Boswell, R., Anderson, B.J., Digert, S.A., Pospisil, G., Baker, R., Weeks, M., 2011. Mount Elbert Gas Hydrate Stratigraphic Test Well, Alaska North Slope: Overview of scientific and technical program. *Journal of Marine and Petroleum Geology* 28 (2), 295–310.
- Inks, T.L., Lee, M.W., Agena, W.F., Taylor, D.J., Collett, T.S., Zyrjanova, M.V., Hunter, R.B., 2008. Seismic prospecting for gas hydrate and associated free-gas prospects in the Milne Point area of northern Alaska. In: *Collett, T., Johnson, A., Knapp, C., Boswell, R. (Eds.), Natural Gas Hydrates—Energy Resource Potential and Associated Geologic Hazards*. AAPG Memoir 89, 1–29.
- Jamison, H.C., Brockett, L.D., McIntosh, R.A., 1980. Prudhoe Bay – a 10 year perspective. In: *Halbouty, M.T. (Ed.), Giant Oil and Gas Fields of the Decade 1986–1978*. AAPG Memoir 30, 289–314.
- Kaufman, D.S., et al., 2004. Holocene thermal maximum in the western Arctic (0–180 °C). *Quaternary Science Reviews* 23, 529–560.
- Krinsley, D.H., Doornkamp, J.C., 1973. *Atlas of Quartz Sand Surface Textures*. Cambridge University Press, Cambridge.
- Krumbein, W.C., Sloss, L.L., 1963. In: *Stratigraphy and Sedimentation*, second ed. W.H. Freeman and Company, San Francisco.
- Kvenvolden, K.A., Lorenson, T.D., 2001. The global occurrence of natural gas hydrate. *Natural Gas Hydrates: Occurrence, Distribution, and Detection*. American Geophysical Union, Washington, DC, pp. 3–18.
- Kwon, T.H., Cho, G.C., Santamarina, J.C., 2008. Gas hydrate dissociation in sediments: pressure–temperature evolution. *Geochemistry, Geophysics, Geosystems* 9 (3). doi:10.1029/2007GC001920.
- Lachenbruch, A.H., Sass, J.H., Marshall, B.V., Moses Jr., T.H., 1982. Permafrost, heat flow, and the geothermal regime at Prudhoe Bay, Alaska. *Journal of Geophysical Research* 87 (B11), 9301–9316.
- Lee, M.W., Collett, T.S., 2011. In-situ gas hydrate saturation estimated from various well logs at the Mount Elbert Gas Hydrate Stratigraphic Test Well, Alaska North Slope. *Journal of Marine and Petroleum Geology* 28 (2), 439–449.
- Lee, J.Y., Yun, T.S., Santamarina, J.C., Ruppel, C., 2007. Observations related to tetrahydrofuran and methane hydrate for laboratory studies of hydrate bearing sediments. *Geochemistry, Geophysics, Geosystems* 8, Q06003. doi:10.1029/2006GC001531.
- Lee, J.Y., Santamarina, J.C., Ruppel, C., 2008. Mechanical and electromagnetic properties of northern Gulf of Mexico sediments with and without THF hydrates. *Marine Petroleum Geology* 25 (9), 884–895.
- Lee, J.Y., Santamarina, J.C., Ruppel, C.D., 2009. Volume change during formation and dissociation of THF hydrate in sediments. *Geochemistry, Geophysics, Geosystems*. doi:10.1029/2009GC002667.
- Lerand, M., 1973. Beaufort Sea. In: *McCrossan, R.G. (Ed.), The Future Petroleum Provinces of Canada – Their Geology and Potential*. Canadian Society of Petroleum Geologists Memoir, 1, pp. 315–386.
- Lo, K.Y., Roy, M., 1973. Response of particulate materials at high pressures. *Soils and Foundations* 13 (1), 61–76.
- Lorenson, T.D., Collett, T.S., Hunter, R.B., 2008. Preliminary assessment of hydrocarbon gas source from the Mt. Elbert No.1 gas hydrate test well, Milne Pt. Alaska. In: *Proceedings of the 6th International Conference on Gas Hydrates (ICGH 2008)*, Vancouver.
- Lunardini, V.J., 1995. Permafrost formation time. *CRREL Report*, 95-8.
- Mahaney, W.C., Kalm, V., 1996. Field Guide for the International Conference on Quaternary Glaciation and Paleoclimate in the Andes Mountains. Quaternary Survey, Toronto.
- Mahaney, W.C., 2002. *Atlas of Sand Grain Surface Textures and Applications*. Oxford University Press, Inc., New York.
- Masterson, W.D., Dzou, L.I.P., Holba, A.G., Fincannon, A.L., Ellis, L., 2001. Evidence for biodegradation and evaporative fractionation in West Sak, Kuparuk and Prudhoe Bay field areas, North Slope, Alaska. *Organic Geochemistry* 32 (3), 411–441.
- Matheus, P., Beget, J., Mason, O., Gelvin-Reymiller, C., 2003. Late Pliocene to late Pleistocene environments preserved at the Palisades Site, central Yukon River, Alaska. *Quaternary Research* 60, 33–43.
- McDowell, G.R., 1999. Micromechanics of clastic soil. In: *Proceedings of the International Workshop on Soil Crushability*, Ube, Yamaguchi, Japan, pp. 138–157.
- Nakata, Y., Hyodo, M., Hyde, A.F.L., Kato, Y., Murata, H., 2001. Microscopic particle crushing of sand subjected to one-dimensional compression. *soils and foundations*. Japanese Geotechnical Society 41 (1), 69–82.
- Osterkamp, T.E., Gosink, J.P., 1991. Variations in permafrost thickness in response to changes in Paleoclimate. *Journal of Geophysical Research* 96 (B3), 4423–4434.
- Parrish, J.M., Parrish, J.T., Hutchison, J.H., Spicer, R.A., 1987. Late Cretaceous vertebrate fossils from the North Slope of Alaska and implications for dinosaur ecology. *PALAIOS* 2 (4), 377–389.
- Pratt, R.M., 1979. Gas hydrate evaluation and recommendations. National Petroleum Reserve, Alaska: U.S. Geological Survey Special Report TC-7916, 27 pp.
- Reimnitz, E., Wolf, S.C., Rodeick, C.A., 1972. Preliminary interpretation of seismic profiles in the Prudhoe Bay area, Beaufort Sea, Alaska. U.S. Geological Survey Open-File Report 72-312.
- Reiser, H.N., Brosge, W.P., Dutro, J.T., Dettelman, R.L., 1978. Geologic map of the demarcation point Quadrangle, Alaska: U.S. Geological Survey Open-File Report 78-526.
- Rhoades, J.D., 1982. Soluble salts, methods of soil analysis. Part 2. Chemical and Microbiological Properties. ASA-SSSA.
- Rose, K., Boswell, R., Collett, T.S., 2011. Mount Elbert Gas Hydrate Stratigraphic Test Well, Alaska North Slope: Coring operations, core sedimentology, and lithostratigraphy. *Journal of Marine and Petroleum Geology* 28 (2), 311–331.
- Santamarina, J.C., Cho, G.C., 2001. Determination of critical state parameters in sandy soils – simple procedure. *ASTM Geotechnical Testing Journal* 24 (2), 185–192.
- Santamarina, J.C., Ruppel, C., 2010. The impact of hydrate saturation on the mechanical, electrical, and thermal properties of hydrate-bearing sand, silts, and clay. In: *Riedel, M., Willoughby, E., Chopra, S. (Eds.), Gas Hydrates, series "Investigations in Geophysics"*.

- Santamarina, J.C., Klein, K.A., Fam, M.A., 2001. *Soils and Waves*. John Wiley & Sons, New York, 488 pp.
- Santamarina, J.C., Klein, K.A., Wang, Y.H., Prencke, E., 2002. Specific surface: determination and relevance. *Canadian Geotechnical Journal* 39 (1), 233–241.
- Sloan, E.D., Koh, C.A., 2008. *Clathrate Hydrates of Natural Gases*. CRC Press, Boca Raton, FL.
- Spicer, R.A., Chapman, J.L., 1990. Climate change and the evolution of high-latitude terrestrial vegetation and floras. *TREE* 5 (9), 279–284.
- Torres, M.E., Collett, T., Rose, K., Sample, J.C., Agena, W., Rosenbaum, E., 2011. Pore fluid geochemistry from the Mount Elbert Gas Hydrate Stratigraphic Test Well, Alaska North Slope. *Journal of Marine and Petroleum Geology* 28 (2), 332–342.
- Valdes, J.R., Santamarina, J.C., 2006. Particle clogging in radial flow: microscale mechanisms. *SPE Journal* 11 (2), 193–198.
- Valdes, J.R., Santamarina, J.C., 2007. Particle transport in a nonuniform flow field: retardation and clogging. *Applied Physics Letters* 90 (24), 244101.
- Valin, Z.C., Collett, T.S., 1992. Molecular and isotopic analyses of the hydrocarbon gases within gas hydrate-bearing rock units of the Prudhoe Bay-Kuparuk River area in Northern Alaska. U.S. Geology Survey, Open-File Report 92-299.
- Winters, W., Walker, M., Hunter, R., Collett, T., Boswell, R., Rose, K., Waite, W., Torres, M., Patil, S., Dandekar, A., 2011. Physical properties of sediment from the Mount Elbert Gas Hydrate Stratigraphic Test Well, Alaska North Slope. *Journal of Marine and Petroleum Geology* 28 (2), 361–380.
- Wolfe, J.A., Upchurch Jr., G.R., 1987. North American nonmarine climates and vegetation during the late Cretaceous. *Palaeogeography, Palaeoclimatology, Palaeoecology* 61, 33–77.
- Wolfe, J.A., 1980. Tertiary climates and floristic relationships at high latitudes in the northern hemisphere. *Palaeogeography, Palaeoclimatology, Palaeoecology* 30, 313–323.
- Wolfe, J.A., 1994. Tertiary climatic change at middle latitudes of western North America. *Palaeogeography, Palaeoclimatology, Palaeoecology* 108, 195–205.
- Yamamoto, J.A., Lade, P.V., 1996. Drained sand behavior in axisymmetric tests at high pressures. *Journal of Geotechnical Engineering, ASCE* 122 (2), 109–119.
- Yun, T.S., Santamarina, J.C., Ruppel, C., 2007. Mechanical properties and rheology of sand, silt, and clay containing synthetic hydrate. *Journal of Geophysical Research* 112, B04106. doi:10.1029/2006JB004484.